A&A 422, 1093–1104 (2004)
DOI: 10.1051/0004-6361:20041001

Astronomy & Astrophysics

On the fine structure of sunspot penumbrae

I. A quantitative comparison of two semiempirical models with implications for the Evershed effect

J. M. Borrero[1], S. K. Solanki[1], L. R. Bellot Rubio[2], A. Lagg[1], and S. K. Mathew[3,1]

[1] Max-Planck Institut für Aeronomie, 37191 Katlenburg-Lindau, Germany
e-mail: borrero@linmpi.mpg.de
[2] Kiepenheuer-Institut für Sonnenphysik, Schöneckstr. 6, 79104 Freiburg, Germany
[3] Instituto de Astrofísica de Canarias, vía Láctea s/n, 38200 La Laguna, Tenerife, Spain

Received 1 April 2004 / Accepted 26 April 2004

Abstract. Sunspot penumbrae exhibit prominent fine structure. Different interpretations of spectropolarimetric observations suggest different, sometimes contradictory, properties of this fine structure. In this paper we show that the results of inversions of penumbral infrared profiles based on one-component models with gradients of the atmospheric parameters and two-component models without gradients are compatible with each other. Our analysis reconciles the results of previous investigations and provides further support for the picture that sunspot penumbrae are composed of penumbral flux tubes embedded in a magnetic background. The magnetic field in the tubes is more horizontal and weaker than that of the background atmosphere. While the tubes carry most of the Evershed flow, the background is essentially at rest. We notice also that the magnetic field strength in the flux tubes drops much more slowly with radial distance than the background field. This finding is discussed as a possible driver for the Evershed flow.

Key words. Sun: sunspots – line: profiles – Sun: magnetic fields – Sun: infrared

1. Introduction

The fine structure of the penumbra has been the subject of many investigations (see Solanki 2003; Bellot Rubio 2003, for recent reviews). Most of these involve high resolution imaging, allowing the horizontal distribution of brightness (and partly of the magnetic field if magnetograms were obtained), and its evolution to be deduced. Spectra and in particular spectropolarimetric measurements, i.e. the full polarization profiles of spectral lines, provide additional, largely complementary information. The full potential of spectropolarimetry is realized when combined with non-linear inversion techniques. This combination allows the line of sight velocity, magnetic field vector and temperature to be determined with high precision and in three dimensions, at the cost of temporal and spatial resolution.

Inversion techniques have played a key role in the interpretation of observations. The first inversion of a complete sunspot was presented by Lites & Skumanich (1990) based on polarization profiles of the Fe I 630.25 nm line obtained with the Stokes II instrument. Subsequently, further inversions of sunspots have been carried out, mostly using the pair of Fe I lines at 630 nm observed by the Advance Stokes Polarimeter (ASP, Elmore et al. 1992). The degree of sophistication of the physical models used in the inversions has increased with time. Until 1997, most inversions of penumbral profiles relied on one-component Milne-Eddington (ME) atmospheres. The ME inversion code of the High Altitude Observatory (Skumanich & Lites 1987) has been successfully used to study the structure of sunspot penumbrae by, among others, Lites & Skumanich (1990), Lites et al. (1993), Stanchfield et al. (1997), and Lites et al. (2002). The first inversion of a penumbra in terms of one-component models with gradients of the atmospheric parameters was carried out by Westendorp Plaza et al. (1997) using the SIR code (Stokes Inversion based on Response functions, Ruiz Cobo & del Toro Iniesta 1992). This code made it possible to investigate the structure of the penumbra in different layers of the photosphere (Westendorp Plaza et al. 2001a,b).

The availability of infrared measurements, mainly the Fe I lines at 1565 nm recorded with the Tenerife Infrared Polarimeter (TIP, Martínez Pillet et al. 1999), made the deeper layers of the sunspot atmosphere accessible. Solanki et al. (1992, 1994) presented the first inversions in this spectral window using numerical solutions of the Radiative Transfer Equation, which allowed the characterization of the magnetic canopy and the Evershed effect. This work was followed by one-component inversions allowing for gradients in the physical parameters (Bellot Rubio et al. 2002; Mathew et al. 2003).

Finally, more complex inversions based on two-component models have been carried out (del Toro Iniesta et al. 2001; Bellot Rubio 2003; Bellot Rubio et al. 2003) which have the potential to partly overcome the problem of the limited spatial resolution.

The results of these investigations of the visible and infrared data support the idea that sunspot penumbrae consist of penumbral flux tubes embedded in a magnetic background (see Bellot Rubio 2003), as proposed by Solanki & Montavon (1993) in their uncombed penumbral model. However, inversions based on visible and infrared lines do not always agree on the properties of the fine structure, and the same is true for inversions based on one-component and two-component models. In extreme cases, opposite tendencies are deduced from visible and infrared lines. The one-component inversions of visible lines performed by Westendorp Plaza et al. (2001a), for example, revealed magnetic field strengths increasing with height in most of the outer penumbra, whereas a similar one-component model applied to infrared measurements results in field strengths decreasing with height (Mathew et al. 2003).

Here we show that the results of one component models with gradients of the atmospheric parameters and of two-component models without gradients are compatible with each other, and that differences between them are more apparent than real. The results of both models provide a possible explanation why the Evershed flow is directed outward in spite of the rapidly decreasing penumbral magnetic field strength. We also offer an explanation for the different behaviors inferred from visible and infrared lines based on the different sensitivity of these lines to the various atmospheric layers. To this end, we invert the same infrared observations (described in Sect. 2) with the same code (described in Sect. 3) in terms of one and two-component models (Sect. 4). The results of these inversions are compared in Sect. 5. A discussion of the reliability of the different physical models is presented in Sect. 6. We address the implications of our results in Sect. 7 and offer a picture for the penumbral fine structure in Sect. 8 that attempts to reconcile the various observations. Finally, Sect. 9 summarizes our findings.

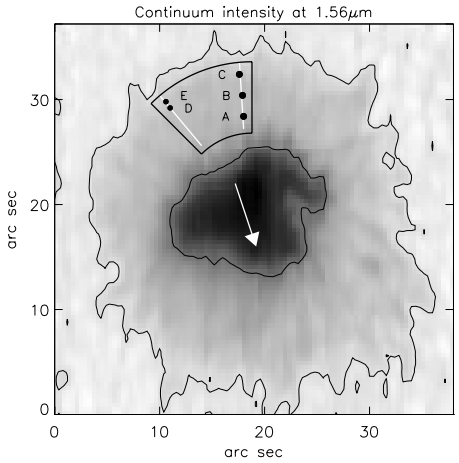

Fig. 1. Continuum intensity image of NOAA 8706 at 1.56 μm. The black box indicates the region in the limb side of the penumbra considered in this work. It is centered on the line connecting the center of the solar disk and of the sunspot (line of symmetry) and spans an interval of 45° in azimuth. Inside it, examples of two radial cuts are plotted in white. The points labeled A, B, and C are three pixels at different radial positions in the penumbra. Points E and D are two consecutive pixels on a different radial cut. The white arrow in the umbra marks the direction to disk center. The two contours indicate the umbra-penumbra and quiet sun-penumbra boundaries. The reference value taken for the sunspot's radius, $r = R$, corresponds to the outer contour at each position angle.

Table 1. Atomic parameters of the observed lines. λ_0 represents the laboratory central wavelength, χ_l the excitation potential of the lower energy level, and $\log gf$ the logarithm of the oscillator strength times the multiplicity of the level. The parameters α and σ (in units of Bohr's radius, a_0) are used to calculate the broadening of the lines by collisions with neutral hydrogen atoms as resulting from the ABO theory. The last column gives the effective Landé factor of the transition, $g_{\rm eff}$.

Species	λ_0 (Å)	χ_l (eV)	$\log gf$ (dex)	α	σ (a_0^2)	$g_{\rm eff}$
Fe I	15 648.515	5.426	−0.675	0.229	977	3.00
Fe I	15 652.874	6.246	−0.043	0.330	1444	1.53

2. Observations

On 27th September 1999, a rather symmetric spot, NOAA 8706, was observed with the Tenerife Infrared Polarimeter (Martínez Pillet et al. 1999) attached to the 70 cm German VTT of Teide Observatory. The spot was located at a heliocentric angle of 24° ($\mu = 0.91$). The recorded spectral region contained the line pair Fe I 15 648 Å and Fe I 15 652 Å, with effective Landé factors of $g_{\rm eff} = 3$ and $g_{\rm eff} = 1.53$ respectively. The seeing conditions were rather good during the observations, with the granulation being clearly discernible in the reconstructed continuum image (Fig. 1). The spatial resolution can be estimated to be about 1 arcsec by calculating the power spectrum of the continuum intensity of the neighbouring granulation. The absolute wavelength scale of the observations was determined using the line core position of the average quiet sun intensity profile of Fe I 15 648 Å and shifting it by 400 m s^{-1}. This value corresponds to the convective blueshift of the line as deduced from the two-component model of Borrero & Bellot Rubio (2002). The telluric blend affecting the red wing of Fe I 15 648 Å was removed by inverting the quiet sun profile of the line and using the fit to determine its shape, which is subsequently extracted from the remaining profiles. The atomic parameters of the observed lines, taken from Borrero et al. (2003a), are summarized in Table 1. Recently, Mathew et al. (2003, 2004) have used the same data set to study the global structure of this sunspot.

3. Inversion procedure

The inversions presented in this work were carried out with the code SPINOR (Frutiger et al. 1999; Frutiger 2000). SPINOR iteratively modifies an initial guess model atmosphere by means of response functions (Ruiz Cobo & del Toro Iniesta 1992) until the synthetic spectrum matches the observed one. The radiative transfer equation is solved in local thermodynamic

equilibrium using the Hermitian algorithm of Bellot Rubio et al. (1998). The continuum absorption coefficient is calculated for a given wavelength, temperature, and electron pressure using the code of Gustaffson (1973) which takes into account contributions from H, He, H^-, He^-, H_2^+, H_2^- and other electron donor species, as well as Rayleigh scattering by H and H_2, and Thompson scattering by free electrons. Several broadening mechanisms are considered: microturbulence, radiative broadening (in the classical damped oscillator approximation), and collisions with neutral hydrogen atoms (for which the ABO theory is employed; see Barklem & O'Mara 1997; Barklem et al. 1998).

Once the emergent spectrum has been computed for a given set of parameters which define the atmosphere, analytical equivalent Response Functions (RFs) are evaluated for the physical stratifications of the model (temperature, line-of-sight velocity, strength, inclination, and azimuth of the magnetic field vector, etc.) at a number of optical depth points called *nodes*. These RFs enter into a Levenberg-Marquardt nonlinear least-squares algorithm (Press et al. 1986) and a new set of parameters at the nodes, able to provide a better fit to the observed profiles, is obtained. New stratifications of the physical parameters along the whole atmosphere are obtained by interpolating the perturbations at the nodes using splines under tension. These steps are repeated until the best fit is achieved. The synthesis and inversion are performed in an optical depth scale, but during each iteration step, the atmospheres are put in hydrostatic equilibrium using the ideal gas law as equation of state.

Inversion techniques (ITs) have been used to investigate many structures of the solar photosphere and chromosphere (for recent reviews see Ruiz Cobo 1998; Socas-Navarro 2001; del Toro Iniesta 2003). The reliability of inversion techniques has been repeatedly demonstrated in the past and we will not discuss this point further (e.g., Westendorp Plaza et al. 1998). However, some words about uniqueness are appropriate at this point. The retrieved results are unique only for the particular geometrical model adopted for the inversion. As long as this model is not changed and is appropriate to the data being inverted (e.g. one could not expect to obtain unique results for the magnetic field vector if only Stokes I is inverted), ITs have proven to be extremely robust and to retrieve the same stratifications of the atmospheric quantities independently of the initial guess. However, the question remains how to understand the results of ITs when different models are adopted to interpret the polarization profiles emerging from sunspot penumbrae. Bellot Rubio (2003) and Leka & Socas-Navarro (2000) have investigated this issue by concentrating on the global properties of the penumbra from the inversion of infrared and visible data respectively. Here we extend this work by focusing our attention on the properties of the penumbral fine structure that result when different geometries are adopted.

4. Geometrical models adopted for the inversion

We have selected two different models for the analysis of the observed penumbral profiles. The first model assumes that in each pixel the fine structure is spatially resolved, so that the shape of the line profiles are due to the height dependence of the thermal, magnetic and kinematic properties of the atmosphere, i.e. temperature T, magnetic field strength B, magnetic field inclination γ and azimuth ϕ (relative to the observer's reference frame) as well as line of sight velocity $v_{\rm LOS}$. In addition, height independent macro- and microturbulent velocities are also obtained through the inversion in order to model those velocities which occur at scales smaller than the resolution element. For each height-dependent physical magnitude we have selected four nodes at the following optical depths: $\log\tau_5 = [1, 0, -1, -2]$[1]. This results in a total of 23 free parameters. Hereafter, this model will be referred to as the *one-component (1C) model*. Similar models have been used to study the structure of sunspots by inverting the polarization signals of Zeeman sensitive spectral lines in the visible (e.g., Westendorp Plaza et al. 1997, 2001a,b) and the infrared (e.g., Bellot Rubio et al. 2002; Mathew et al. 2003).

The second model considers two independent atmospheric components for each spatial pixel, thereby allowing for the possibility that there are horizontal inhomogeneities at scales below the spatial resolution. In order to keep the number of free parameters within reasonable limits, the physical magnitudes describing each component are assumed to be height independent, except for the temperature. In addition to the kinematic and magnetic parameters mentioned above, a filling factor α_t (fractional area of the resolution element covered by the second component) is obtained from the inversion. Here we have a total number of 18 free parameters. In the following this model will be referred to as the *two-component (2C) model*. Bellot Rubio et al. (2003) have used the same physical description of the penumbra to confirm that the Evershed flow is aligned with the magnetic field vector in deep photospheric layers.

In all inversions we use a stray light correction. The stray light intensity profile, $I_{\rm q}$, is taken to be that emerging from the quiet sun according to the two-component model of Borrero & Bellot Rubio (2002). A stray light factor $\alpha_{\rm q}$ is used to combine the stray light profile with the polarization profiles emerging from the 1C and 2C models. $\alpha_{\rm q}$ is a free parameter of the inversion and is included in the total number of free parameters given above. In this way, the synthetic profiles used to fit the observations can be expressed as

$$\boldsymbol{S}_{\rm 1C}(\lambda) = \alpha_{\rm q}\boldsymbol{S}_{\rm q}(\lambda) + \Big(1-\alpha_{\rm q}\Big)\boldsymbol{S}_{\rm p}(\lambda) \tag{1}$$

$$\boldsymbol{S}_{\rm 2C}(\lambda) = \alpha_{\rm q}\boldsymbol{S}_{\rm q}(\lambda) + \Big(1-\alpha_{\rm q}\Big)\Big[(1-\alpha_{\rm t})\boldsymbol{S}_{\rm p1}(\lambda) + \alpha_{\rm t}\boldsymbol{S}_{\rm p2}(\lambda)\Big]$$

where the Stokes vector is defined as $\boldsymbol{S} = (I, Q, U, V)$. $\boldsymbol{S}_{\rm p}$ stands for the synthetic profiles emerging from the penumbral atmosphere of the 1C model, $\boldsymbol{S}_{\rm p1}$ and $\boldsymbol{S}_{\rm p2}$ refer to the two magnetic components of the 2C model. The quiet sun contribution (stray light) is assumed to be unpolarized: $\boldsymbol{S}_{\rm q} = (I_{\rm q}, 0, 0, 0)$.

[1] The assignment of the number and position of the nodes was done by concentrating on those layers to which these lines are sensitive (i.e. calculating the Response Functions). Examples of RF's for these lines can be found in Mathew et al. (2003).

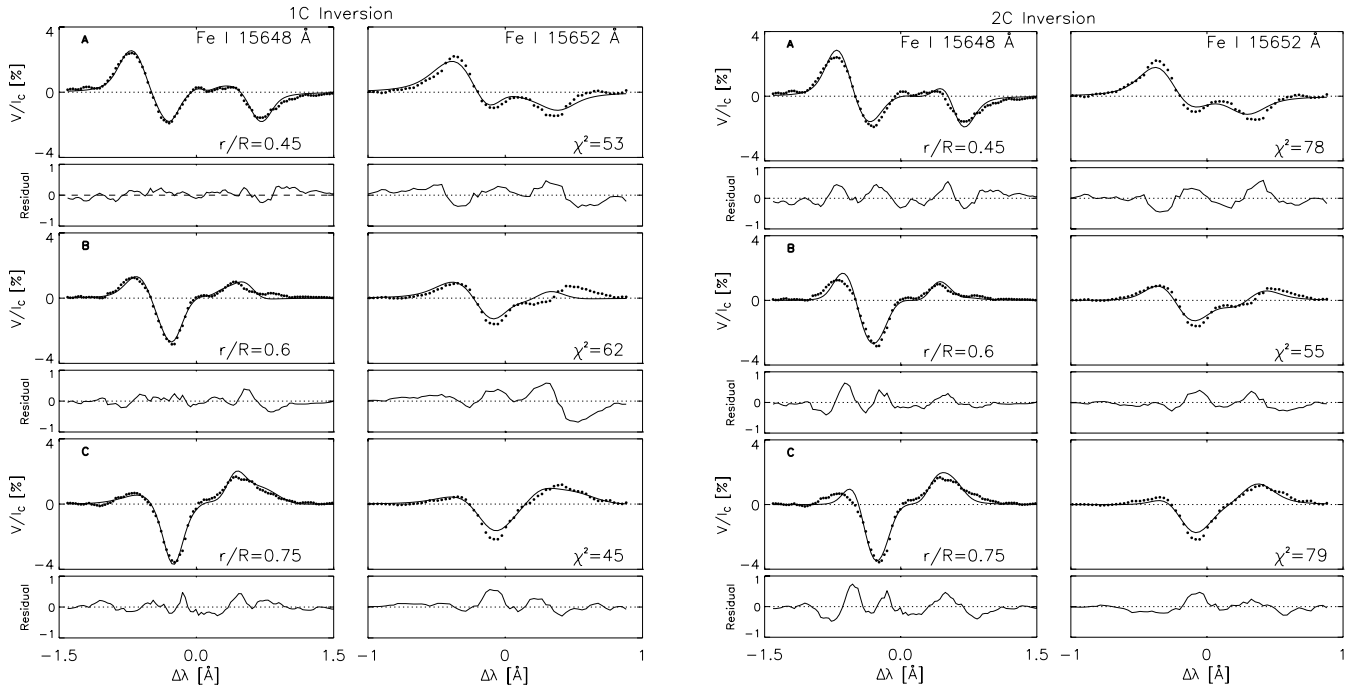

Fig. 2. *Top to bottom*: observed Stokes V profiles (filled circles) corresponding to the points marked as A, B and C in Fig. 1. *Left six panels*: results from the inversions based on the 1C model. *Right six panels*: as before but for the 2C model. The best-fit profiles resulting from the inversions are represented by the solid lines. Beneath each panel showing the V/I_C profile is plotted the difference between observed and best fit profiles (residuals). The χ^2 value is given for each fit. More weight was given during the inversion to the circular polarization than to the total intensity and linear polarizaion. Relative weights were the same in the 1C and 2C inversion.

5. Results

We have inverted all 750 pixels in the region bounded by the thick black lines in Fig. 1, covering r/R values roughly between 0.4 and 0.8, where R denotes the radius of the sunspot in the continuum map. The inverted pixels lie on the limbside penumbra close to the line of symmetry of the spot, i.e., the line connecting the sunspot center with the center of the solar disk. In Fig. 2 we plot three examples of observed Stokes V profiles along with the best-fit profiles resulting from the 1C and 2C inversions. These examples correspond to points A, B, and C in Fig. 1. Near the magnetic neutral line, the observed circular polarization profiles show three or more lobes. The fits, although not perfect, are reasonably successful given the simplicity of the two models. Residuals are always below 0.5% (compared to an approximate noise level of 0.05%). Although in general the 1C model leads to slightly better fits in terms of the final χ^2 values, the difference is not sufficiently large to declare this model more realistic, in particular since the 2C model uses fewer free parameters. The fits to the other Stokes parameters are equally good (not shown).

In Fig. 3 we present the kinematic and magnetic stratifications as a function of the optical depth (for a wavelength reference of 5000 Å: τ_5) of the atmospheres inferred from the inversion of the profiles shown in Fig. 2. The atmospheres corresponding to the 1C model (dashed lines) consistently show large red shifted velocities in high layers (around $\log\tau_5 \simeq -1$), while in deep layers velocities are negligible or even directed towards the observer, although comparatively weak in magnitude. Both, the magnetic field strength and its vertical gradient decrease from the inner to the outer penumbra. Large values ($\gamma \sim 110°$) of the magnetic field inclination in high layers along with smaller ones ($\gamma \sim 60{-}80°$) in deep layers are inferred. The parameters of the two penumbral components returned by the 2C inversion are also indicated in Fig. 3 by horizontal solid lines. It can be seen that one of these atmospheres (#2) has moderate magnetic fields ($B \sim 1200$ G), high inclination angles ($\gamma \sim 100{-}110°$) and large redshifted velocities ($v_{\rm LOS} \sim 1.5{-}2$ km s^{-1}), while the other component (#1) is characterized by stronger ($B \sim 1500{-}2000$ G) and less inclined ($\gamma \sim 60{-}70°$) magnetic fields. In component #1, the line-of-sight velocity is nearly zero. This figure also indicates a similarity between the values returned by the 1C inversion at $\log\tau_5 = -1$ and 0 and the 2C inversion results for component #2 and #1, respectively.

Next we test these hints in a statistically more robust fashion. For all the pixels we have selected the optical depths marked in Fig. 3 with vertical dotted lines ($\log\tau_5 = 0$ and $\log\tau_5 = -1$), extracted the values of the atmospheric parameters from the 1C inversion there and plotted them as a function of radial distance in the penumbra in Fig. 4 (left panels) . The corresponding values for the two atmospheres of the 2C inversions are shown as well (right panels). In this figure, the magnetic field inclination is expressed in the local reference frame. Thus, instead of γ we plot the zenith angle ζ. A zenith angle of zero indicates fields pointing outwards perpendicularly to the solar surface.

At $\log\tau_5 = -1$ the magnetic field returned by the 1C model becomes more horizontal in the middle penumbra

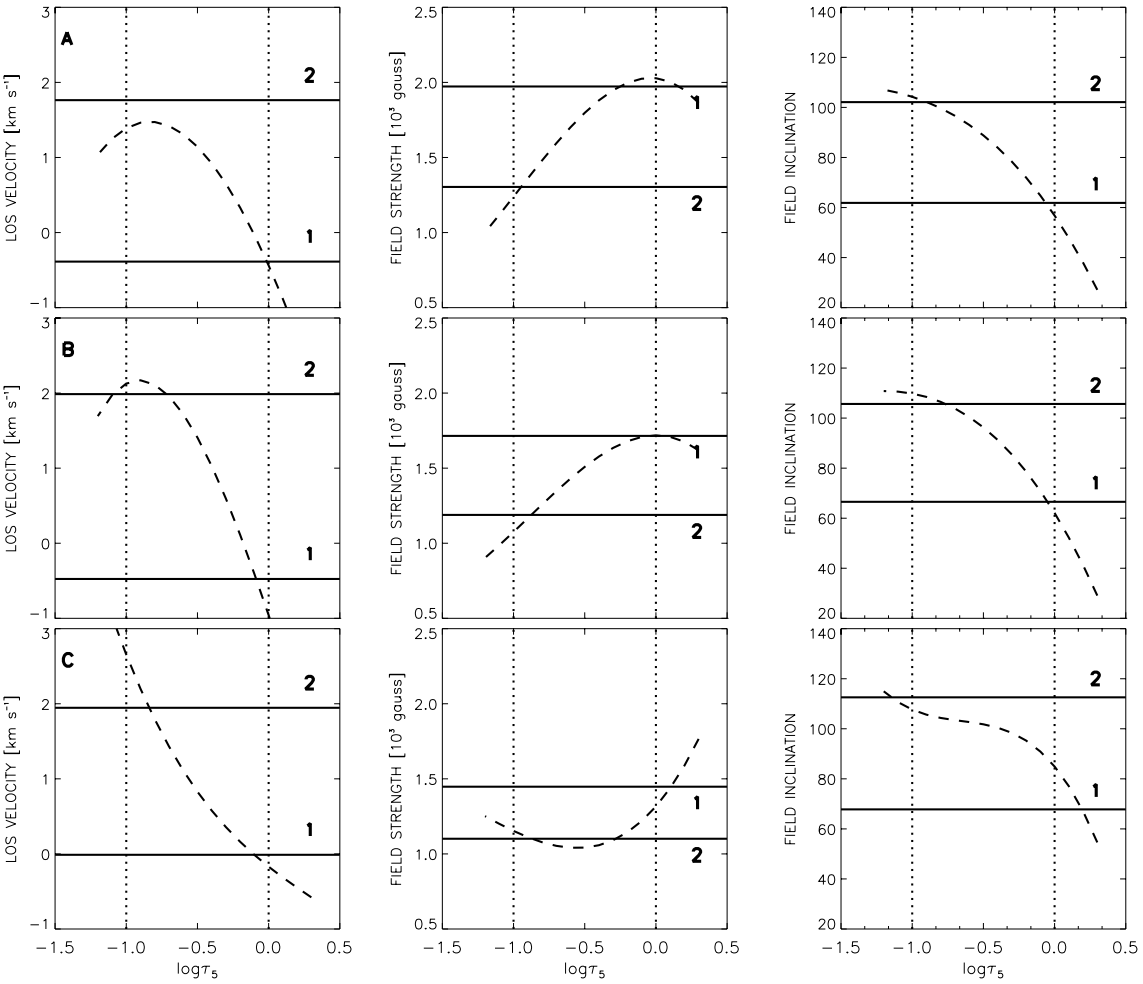

Fig. 3. Examples of atmospheric stratifications resulting from the 1C and 2C inversions (dashed and solid lines, respectively). The numbers next to the solid lines indicate the corresponding magnetic component. *From top to bottom*: results for pixels A, B, and C (see text and caption of Fig. 1 for details). *From left to right*: line-of-sight velocity, magnetic field strength, and magnetic field inclination. The two vertical dotted lines mark the optical depth points selected for further analysis ($\log \tau_5 = 0$ and $\log \tau_5 = -1$). Positive velocities indicate redshifts.

and eventually reaches values slightly larger than 90°, implying that the magnetic field returns to the solar surface. The field strength decreases only slowly with radial distance, whereas the LOS velocities are redshifted and increase radially. At $\log \tau_5 = 0$ we see a rather vertical magnetic field in the inner penumbra which gradually becomes more inclined, although it is never completely horizontal. In this layer, the magnetic field is stronger than at $\log \tau_5 = -1$ in the inner penumbra, but rapidly decreases to similar values at the outer part of the penumbra. The velocity here is almost zero, indicating that the Evershed flow is mostly concentrated in the upper part of the atmosphere.

The 2C inversions show a strikingly similar overall picture. In particular, one of the components (#2) possesses more horizontal, weaker fields whose strength remains more or less constant with radial distance. This component also carries a large flow, whose magnitude increases radially, although by only a small amount. Component #1 is characterized by more vertical and stronger magnetic fields and small LOS velocities. The field strength in this atmospheric component decreases quickly with radial distance.

These two components or layers can be identified with horizontal magnetic flux tubes (carrying the Evershed flow) embedded in a more vertical background (e.g., Solanki & Montavon 1993; Schlichenmaier et al. 1998a,b; Martínez Pillet 2000; Bellot Rubio et al. 2002, 2003; Mathew et al. 2003). Thus, the atmosphere represented by dashed lines in Fig. 4 corresponds to the flux tubes and the atmosphere indicated by solid lines to the background. The correspondence between 1C and 2C inversions is not always perfect. For example, the inclination of the background in the 1C model increases by roughly 20−30° as r/R increases, while it remains unchanged in the 2C inversions. However, these differences do not detract from the remarkable similarity of the behaviors deduced from both models.

One peculiarity of the 1C inversions is a sudden change of the sign of the gradients of LOS velocity and magnetic field inclination at a given radial position. In Fig. 5 this behavior is illustrated for the two consecutive points along the same

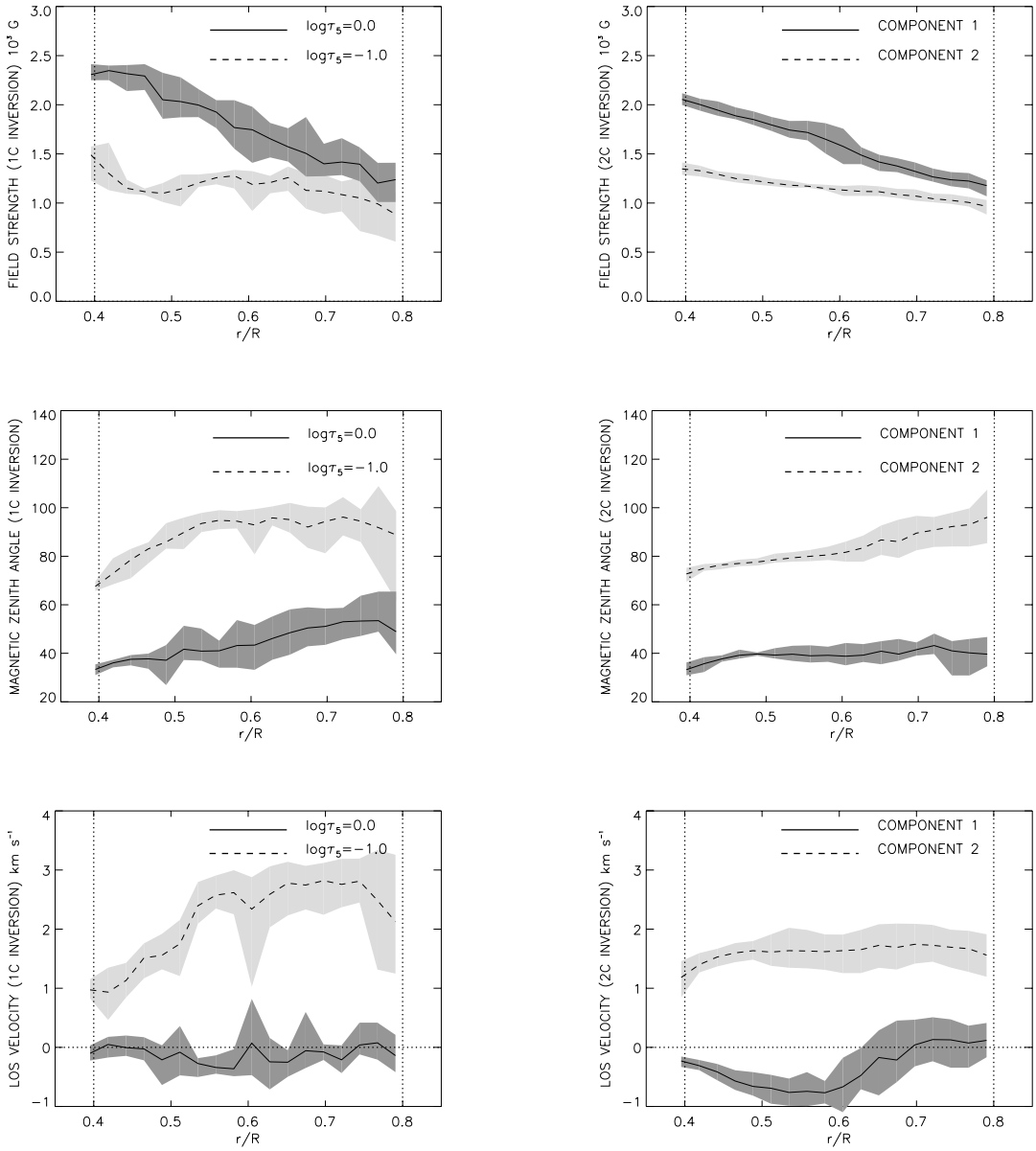

Fig. 4. Radial variation of the inferred physical quantities. *Top panels*: magnetic field strength. *Middle panels*: magnetic zenith angle. *Bottom panels*: line-of-sight velocity. The results of the 1C inversions are shown in the left panels. For these inversions we extract the values at $\log\tau_5 = 0$ (solid lines) and $\log\tau_5 = -1$ (dashed lines). The 2C results are plotted in the right panels. Component #1 (the background) is represented by solid lines, whereas dashed lines correspond to component #2 (flux-tube atmosphere). Solid and dashed lines are averages over all the points at the same radial distance, while the shaded areas correspond to the maximum individual deviations. The 1C results have been corrected (for $r/R \gtrsim 0.75$) by interchanging the values at $\log\tau_5 = -1$ and $\log\tau_5 = 0$ where necessary (see text for details).

radial cut marked D and E in Fig. 1. Whereas in point D the flux tube is better identified with $\log\tau_5 = -1$ this is no longer the case in point E, where it seems appropriate to identify the background with this optical depth position and to shift the flux tube to $\log\tau_5 = 0$, where the horizontal Evershed flow would now be located. All considered radial cuts show this tendency in the outer penumbra. We have corrected for this shift in Fig. 4 by simply interchanging the values of the atmospheric parameters at $\log\tau_5 = 0$ and $\log\tau_5 = -1$ where necessary. One may speculate that the shift is due to the flux tubes sinking back into the photosphere at large radial distances, so that they should be observed in deeper layers as the outer penumbral boundary is approached. Such an explanation is consistent with the retrieved zenith angles which, for the flux tubes, increase radially and finally become larger than 90°. We note here that Mathew et al. (2003) found a similar behavior. They detected large LOS velocities in high layers and small velocities in the deep photosphere for the inner penumbra, but the opposite behavior in the outer penumbra. The uncombed-like inversions of Bellot Rubio (2003) also suggest that the flux tubes are located at increasingly lower layers in the outer penumbra (from $r/R \sim 0.75$ outwards), although this tendency is not well marked.

Before discussing the results and their implications in the next sections, we need to address why the results presented in Fig. 4 are based on the inversion of a region restricted to the limb-side penumbra. The reason for this is the greater coherence and reliability of the results obtained from the profiles

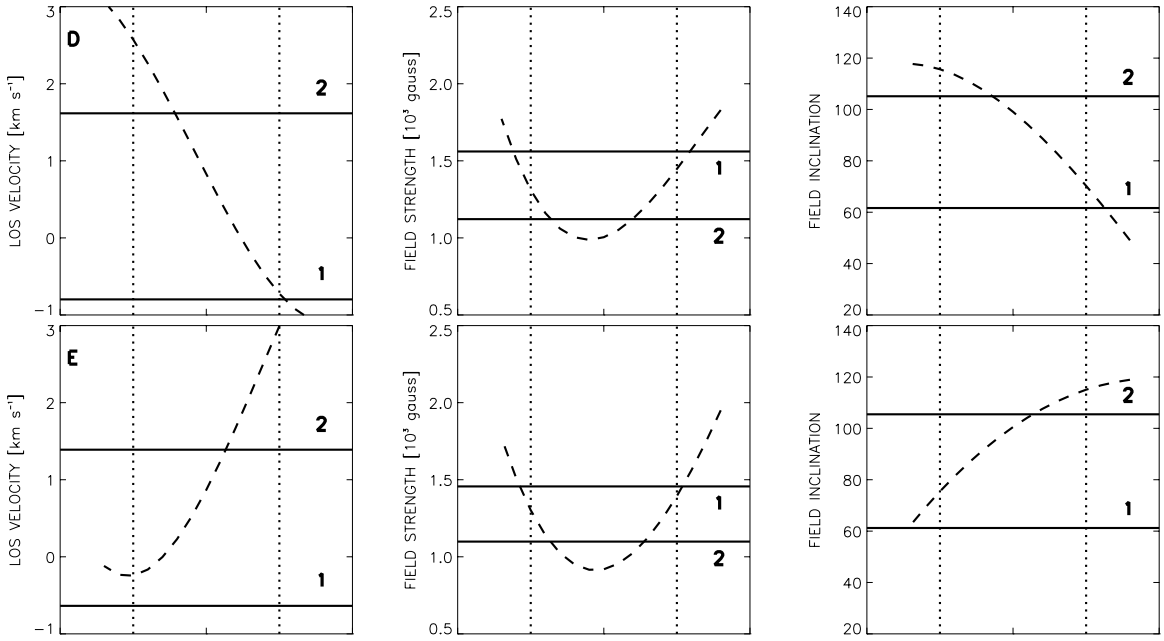

Fig. 5. Atmospheric stratifications derived from the 1C inversion (dashed lines) and 2C inversion (solid lines) of two consecutive radial points referred to as D and E in Fig. 1. Note the sudden change in the gradient of the LOS velocity and field inclination from point D to E.

observed in this region when compared with those at the center side. A possible explanation for the smaller reliability of the 2C inversion results in the center side could be that, in this region, the magnetic field vector in both flux tubes and magnetic background has the same polarity with respect to the line of sight ($\gamma < 90°$), so that both atmospheres give a similar signature and the resulting Stokes V profiles are two lobed. The information carried by the two different components in the circular polarization is then mixed together, making its separate inference more difficult.

To test this idea we have created synthetic data and inverted them for different positions in a hypothetical sunspot. The model underlying the calculation of the synthetic profiles is basically the uncombed model of Solanki & Montavon (1993; see also Borrero et al. 2003b), with the parameters indicated in Table 2. These profiles are then inverted using 10 random initial 2C models (as described in Sect. 4) whose results are presented in Fig. 6. In the limb side we have mixed polarities: flux tube with $\gamma > 90°$ (dashed lines) and background with $\gamma < 90°$ (dotted lines). The 2C inversion recovers both structures almost perfectly in this case. However, in the center side the polarities are the same ($\gamma < 90°$) and the 2C inversion recovers the original stratifications with larger uncertainties. This supports the explanation proposed above. Note that this conclusion is based on the behavior showed by the circular polarization profiles in different regions of the spot. It could well be that, under the appropriate viewing angles, the different signature of the two components in the center-side penumbra appear mostly in the linear polarization (Stokes Q and U) profiles. For example, if a sunspot is observed near the limb ($\theta \simeq 40°$), the background magnetic field in the center side of the penumbra would be aligned with the observer ($\gamma_B = 0°$) and would not produce any linear polarization signal; thus, allowing for a better distinction of the different components when inverted with a 2C model. This idea must be confirmed by inverting a wider sample of sunspots at different heliocentric angles.

Table 2. Physical parameters of the uncombed field model used for the numerical test. Index T refers to a flux tube which is embedded in a background (index B). B and γ are the strength and inclination of the magnetic field vector (with respect to the observer) respectively. V_{LOS} is the line of sight velocity. α_T and α_Q have the same meaning as in Eq. (1). R_T is the flux tube's radius and z_0 is its central position. The uncombed model is basically a modified 2C model where the B component is a pure penumbral background field with no height variation is the physical parameters. The component T has the same stratifications than the latter except between $z_0 - R_T$ and $z_0 + R_T$ where the tube is located and where physical magnitudes suffer a jump (from index B to T, e.g., solid line in Fig. 6). In the local reference frame $\zeta_B = 60°$ and $\zeta_T = 90°$ are chosen. However in the observer's frame we have $\gamma = \zeta + \theta$ on the limb side or $\gamma = \zeta - \theta$ on the center side, where $\theta = 25°$ as in our observations.

Parameter	Units	Outer center side	Outer limb side
B_B	Gauss	1000	1000
γ_B	deg	35	85
$V_{LOS,B}$	km s^{-1}	0	0
B_T	Gauss	1000	1000
γ_T	deg	55	115
$V_{LOS,T}$	km s^{-1}	−2.75	2.00
α_T		0.65	0.65
R_T	km	150	150
z_0	km	100	100
α_Q		0.15	0.15

6. Stokes *V* area asymmetry

A potentially powerful diagnostic of the penumbral fine structure that has not been considered in the previous section is

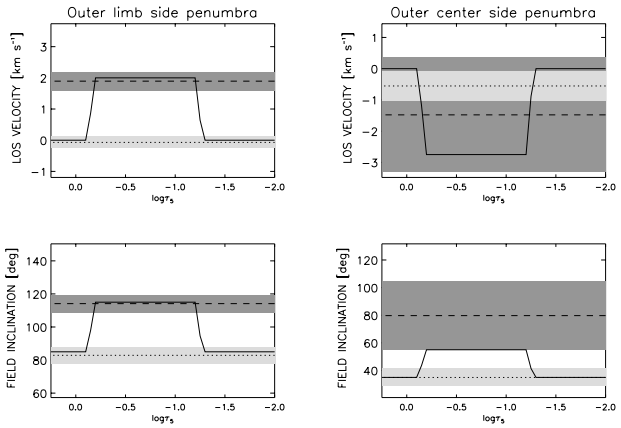

Fig. 6. Stratifications of LOS velocity (*upper panels*) and magnetic field inclination (*lower panel*) for two hypothetical points in the outer ($r/R > 0.7$) limb side (*left panels*) and center side (*right panels*) of the penumbra. Dotted and dashed lines are the results obtained by applying a 2C inversion to the profiles synthesized with the uncombed model (solid lines; see also Table 2). The shaded areas represent the standard deviations corresponding to 10 random initializations.

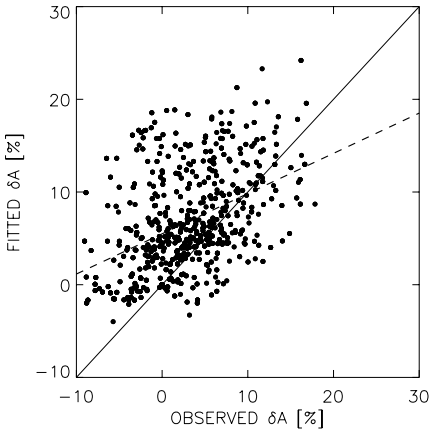

Fig. 7. Area asymmetry, δA, of the best-fit Stokes V profiles vs. the observed δA. The mean δA is around 3% and 7% for the observed and best-fit profiles, respectively. The solid line represents the expectation value, while the dashed line is a linear fit to the points.

the Stokes V area asymmetry, δA. Observations show that δA, defined as

$$\delta A = \frac{\int V(\lambda)\,\mathrm{d}\lambda}{\int |V(\lambda)|\,\mathrm{d}\lambda}, \tag{2}$$

is non-zero in the penumbra for both visible and infrared spectral lines (Illing et al. 1974a,b; Makita 1986; Sánchez Almeida & Lites 1992; Schlichenmaier & Collados 2002; Schlichenmaier et al. 2002; Müller et al. 2002). While the 2C model used here possesses height independent magnitudes (e.g., B, γ, $V_{\rm LOS}$), so that it is unable to produce asymmetric profiles, the 1C model incorporates such height variations (i.e. gradients). To test how well the 1C inversion reproduces the observed area asymmetries we plot in Fig. 7 the Stokes V area asymmetry of the best-fit Fe I 15 648 and 15 652 Å profiles resulting from the 1C inversion versus the observed values. Figure 7 shows that the observed δA is small, with values never exceeding 20% [2], in contrast to the visible lines at 6300 Å where larger values are quite common (Westendorp Plaza et al. 2001a). This figure also shows that the 1C model tends to overestimate the observed area asymmetry (see linear fit). The reason for the large scatter is basically the small sensitivity of these infrared lines to line-of-sight gradients in the atmospheric parameters together with the oversimplified picture of the real penumbral structure represented by the 1C model. To demonstrate this we construct a magnetic atmosphere similar to those obtained from the 1C inversion (see Fig. 3) but where the gradients are substituted by a step-like jump in the stratifications of the physical magnitudes at a prescribed level τ_0. This jump is similar to the one present at the lower boundary of a horizontal flux tube carrying the Evershed flow (see Fig. 8a). A constant magnetic field with $B = 1500$ G, $\gamma = 70°$, $\phi = 0°$ and no flows are assumed below τ_0 to simulate a background with properties similar to those in Fig. 3. For the flux tube (layers above τ_0) we adopt the following values: $B = 1000$ G, $\gamma = 115°$, $\phi = 0°$ and $V_{\rm LOS} = 1.75$ km s^{-1}. The temperature stratification is taken from the penumbral model by del Toro Iniesta et al. (1994). Stokes V profiles and δA values are computed for the two analyzed infrared lines 15 648 and 15 652 Å as well as the widely used pair of lines Fe I 6301 and 6302 Å. This is done for τ_0 values ranging between 10^{-5} and 10. Obviously, for a line formed in the height range $\tau = [\tau_{\rm u}, \tau_\ell]$, a non-zero δA will be obtained only when the discontinuity τ_0 is located between $\tau_{\rm u}$ and τ_ℓ (see Fig. 8a). The results are presented in Fig. 8b. The δA of the visible lines is much more sensitive to discontinuities along the line of sight than that of the infrared lines. Indeed, the lines used in this work are almost insensitive to such discontinuities, exhibiting some area asymmetry ($\delta A_{\rm max} \sim 10\%$) only in a very narrow range of optical depths (from $\log\tau_5 \sim -1$ to $\log\tau_5 \sim 0$, with a maximum around $\log\tau_5 \sim -0.2$). As explained by Landolfi & Landi degl'Innocenti (1996) and Grossmann-Doerth et al. (1989) this results follows directly from the properties of the lines (Landé factors, saturation). From these results we draw the following conclusions:

- The formation of the Fe I 15 648 and 15 652 Å lines is dominated by the presence of two opposite polarities in the resolution element. Successful fits can be achieved with the help of the 2C model because the lines are only slightly influenced by discontinuities[3].
- The visible Fe I 6301 and 6302 Å lines are strongly influenced by discontinuities, which gives rise to large δA values. Successful fits to those kind of profiles can only be

[2] We estimate that a noise level of $5 \times 10^{-4}\, I_C$ in the observed circular polarization can introduce a maximum bias of ±1% in the observed δA, so that this cannot be the cause of the relatively poor correspondence.

[3] As pointed out by Müller et al. (2002) and Schlichenmaier et al. (2002), δA for Fe I 1.56 μm lines is dominated by the jump in azimuths between the flux tube and background. Assuming $\Delta\phi = 0$ is justified as long as our studied region is near the line of symmetry of the sunspot. We have checked that , as expected, δA for the infrared lines changes when $\Delta\phi \neq 0$, but remains smaller than in the visible lines.

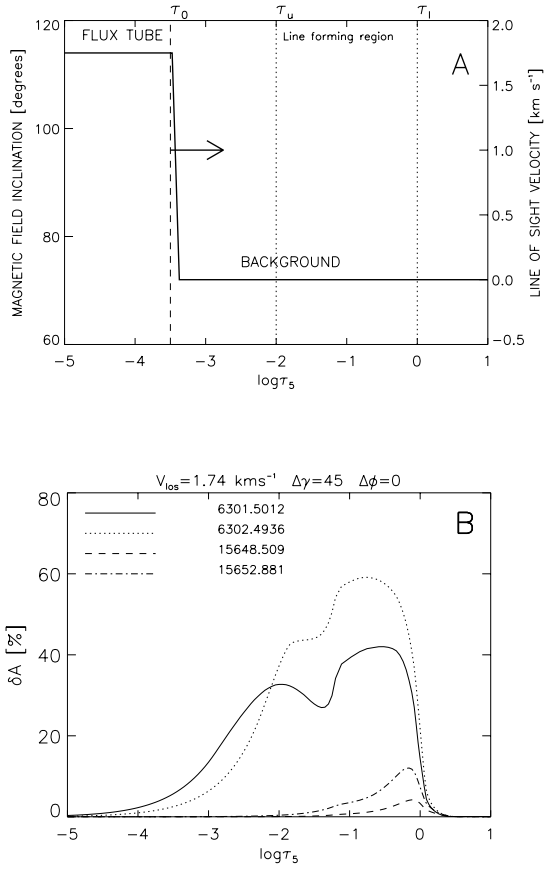

Fig. 8. a) Illustration of the method employed to determine the sensitivity of the Stokes V area asymmetry to discontinuities of the physical parameters along the line of sight. The thick solid line corresponds to a possible stratification including a flux tube. The vertical dashed line marks the position of the boundary τ_0 which is displaced following the arrow. The vertical dotted lines limit the formation region for a generic spectral line. **b)** Stokes V area asymmetries resulting from the calculations of two visible and two infrared neutral iron lines. For the infrared lines, $\delta A_{\max} \simeq 10\%$ and the range of sensitivity is $\log\tau \in [0,-1]$. Visible lines are much more affected by the discontinuity in a wider optical depth range. The maximum area asymmetry of the visible lines occurs when the discontinuity is placed at higher layers than in the case of the infrared lines.

achieved by means of models including gradients (e.g. our 1C model), or discontinuities.

- The stratifications inferred from the 1C inversions, the observed Stokes V area asymmetry of the iron lines at 1.56 μm, and the results from the numerical experiment suggest that at least in the inner penumbra these lines detect the lower boundary of the horizontal flux tube. This needs to be confirmed by inversions with a more realistic model.
- The wider formation height range of visible lines may allow to detect both tube's boundaries if its width does not exceed 250−300 km and if it lies entirely above $\tau_5 = 1$ in the photosphere.

7. Magnetic flux tubes and the Evershed flow

One of the most interesting result of our analysis concerns the radial variation of the magnetic field strength (top panels in Fig. 4). Whereas the strength in the more vertical component (component #1 in the 2C inversion or $\log\tau_5 = 0$ level in the 1C inversion) drops rapidly from the inner to the outer penumbra, the field strength of the flux tube component decreases very slowly (component #2 of the 2C model or $\log\tau_5 = -1.0$ level in the 1C model). Roughly speaking, B changes only from ∼1300 G in the inner penumbra (where upflows are present) to ∼1000 G in the outer penumbra (where downflows dominate; $\zeta > 90°$). A small radial decrease of the field strength in the flux tube was also obtained by Bellot Rubio (2003) from both 2C inversions and uncombed-like inversions of another spot[4]. However, this effect has passed unnoticed in previous 1C analyses.

To understand why, it is important to recall the limitations of the empirical models typically employed to analyze sunspot spectropolarimetric data. Generally only one atmosphere is assumed to be present in the resolution element and all atmospheric parameters are taken to be constant with height. Such models provide a horizontal and vertical average (over the resolution element and the height range of formation of the lines, respectively) of the magnetic and kinematic properties of the different penumbral structures. Thus, deduced field strengths generally drop from ∼2000 G in the inner penumbra to ∼1000 G at the outer penumbral boundary (Lites & Skumanich 1990; Solanki et al. 1992; McPherson et al. 1992; Lites et al. 1993; Keppens & Martínez Pillet 1996; cf. Solanki & Schmidt 1993).

This large decrease of the magnetic field strength has long been considered to present a major difficulty for explaining the Evershed effect in terms of a siphon flow whose downflowing footpoint lies within the penumbra. In the last decade it has become clear that most of the mass carried by the Evershed flow emerges first in the inner part of the penumbra and returns below the solar surface at the outer penumbral boundary (Solanki et al. 1994, 1999; Westendorp Plaza et al. 1997).

Siphon flow models, according to which the Evershed flow is driven by the gas pressure difference between the two footpoints (Meyer & Schmidt 1968; Degenhardt 1989; Thomas 1988; Thomas & Montesinos 1990, 1991; Montesinos & Thomas 1993, 1997), require the opposite behavior, that is, larger magnetic fields in the (outer) downflowing footpoint than in the (inner) upflowing footpoint. In fully dynamic models a similar behavior is found (Schlichenmaier 2002; cf. Schlichenmaier et al. 1998a,b) if mass return is to be present within the penumbra. Montesinos & Thomas (1997) have argued that differences in the geometrical height at which the magnetic field is measured in the inner and outer penumbra can make the observed field in the downflowing footpoint appear smaller, while in reality it is larger. This hypothesis remains to be proven for realistic sunspot models (Solanki 2003).

[4] The term uncombed-like inversions refer to a two component model where a Gaussian function is used to represent the discontinuities along the line of sight in the physical magnitudes. This mimics the step function used in Fig. 6. The central position and width of the Gaussian would be equivalent to the central position Z_0 and radius R_T of the penumbral flux tubes as in the uncombed model from Solanki & Montavon (1993) in Table 2.

In agreement with the results obtained from Ti I 2.2 μm lines by Rüedi et al. (1998, 1999), our inversions show a slowly decreasing (almost constant) field strength inside the (almost) horizontal magnetic component carrying the Evershed flow (flux tube). This result removes one of the main hurdles facing the siphon flow mechanism and reduces the need to invoke changes in the height of the observed layers within the penumbra (Montesinos & Thomas 1997). Thus, most of the magnetic flux in the penumbra exhibits the strong reduction in field strength with radial distance required to attain a magnetohydrostatic equilibrium. The small part of the magnetic flux supporting the Evershed flow is almost independent of radial distance, however. An investigation involving a more realistic geometry of the penumbral magnetic field, including constraints on the pressure gradients within the flux tubes will be the subject of another paper (Borrero et al. 2004, in preparation).

8. A picture for the penumbral fine structure

In Sect. 5 we have seen that the atmospheric parameters resulting from the 1C and 2C inversion show essentially the same behavior: a weaker, more horizontal field supporting the Evershed flow (flux tubes) coexists with a stronger, more vertical field containing gas that is essentially at rest (background). From a geometrical point of view, however, the two models are significantly different. In the 1C model the flux tube lies on top of the background, while in the 2C model, both structures coexist next to each other, without any vertical interlacing. It is not straight forward to decide, on the basis of the present data, which model comes closer to reality. On the one hand, the 1C model is able to provide slightly better fits to the observed profiles while the inversions based on the 2C model show smoother radial variations (see Fig. 4). However, it is important to recall that, for comparison purposes, we have defined two (somewhat arbitrary) fixed optical depths in the 1C model to extract the atmospheric parameters. It is likely that a different or more dynamic selection of these two points produces smoother radial variations for the 1C model. On the other hand, an advantage of the 2C inversions is that the physical meaning of the two components is very intuitive, whereas in the 1C inversions the two structures are described by the same atmosphere. In addition, the 1C model presents large gradients in the magnetic field inclination with height which are likely to produce unrealistically large magnetic curvature forces (Solanki et al. 1993). However, these gradients are an essential ingredient of the model, needed to produce asymmetric Stokes V profiles. Nevertheless, the observed Stokes V area asymmetry of the 1.56 μm lines is so small that it does not by itself completely rule out the 2C model.

Westendorp Plaza et al. (2001a,b) used a 1C model applied to visible 630 nm Fe I lines and found LOS velocities and magnetic field inclinations decreasing with height, but field strengths increasing with height. From the application of a similar 1C inversion but applied to the infrared 1.56 μm Fe I lines we have obtained (see also Bellot Rubio et al. 2002; Mathew et al. 2003) field strengths that decrease and velocities and magnetic field inclination angles that increase with height As discussed in Mathew et al. (2003) all these results are consistent if visible lines are assumed to sample the upper boundary of the penumbral flux tubes (arrow labeled 1C-VISIBLE in Fig. 9) while infrared lines, more sensitive to deep layers, sample the lower boundary (arrow 1C-INFRARED in Fig. 9). In addition, the results returned by the 2C model in this work (see also del Toro Iniesta et al. 2001; Bellot Rubio 2003; Bellot Rubio et al. 2003) provide information on the flux tubes and the background fields (2C-No. 1 and 2C-No. 2 arrows). Note, however, that this picture needs to be tested using a more realistic model incorporating a magnetic flux tube.

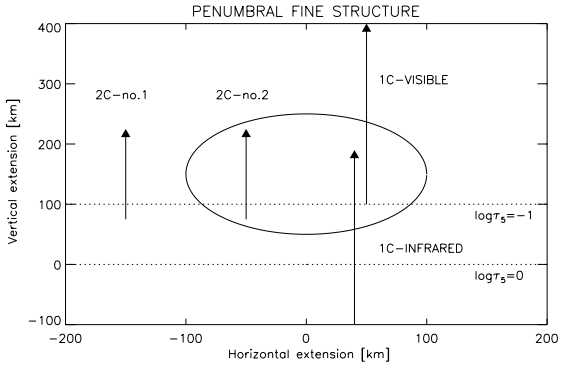

Fig. 9. Sketch of the fine structure of the penumbra. A vertical slice through the penumbra in a direction perpendicular to the fibrils is shown. The oval structure is a cross-section of the flux tube (its shape is of no consequence for the present discussion). The different arrows mark the structures and layers to which the results of 1C inversions with gradients of the atmospheric parameters (*right arrows*) and 2C inversions without gradients (*left arrows*) of visible and infrared lines should be ascribed. See text for details.

9. Summary

We have studied the structure of sunspot penumbrae by means of spectral line inversions considering two different geometries. The first model assumes a one-component atmosphere where all physical parameters are allowed to change with height, while the second model consists of two independent, horizontally interlaced magnetic components whose velocities and magnetic vectors are constant with height. We have shown that both models provide very similar results featuring an almost horizontal magnetic field with a strength of about 1200 G which remains almost constant with radial distance and carries the Evershed flow. This field is inclined slightly upwards in the inner penumbra, is horizontal in the middle penumbra and is inclined downwards at large radial distances. This relatively weak field neighbours a strong (up to $\simeq$2000 G) and more vertical one (zenith angle, $\zeta \simeq 40^\circ$). The strength of the stronger field decreases rapidly with radial distance, becoming almost identical to that of the weaker field in the outer penumbra. No clear signature of the Evershed flow is found in this stronger, more vertical field. The small radial decrease of the magnetic field strength in the component carrying the Evershed flow significantly reduces a major hurdle facing the siphon flow mechanism as the driver of the Evershed effect.

Although the two models lead to the same basic results, they are significantly different from a geometrical point of view. While in the 1C model the weaker field overlies

the stronger one, in the 2C model they lie side by side. Consequently, the 1C model includes gradients along the line of sight. In the second model, no gradients are present because the two components do not interlace vertically. Such gradients or discontinuities along the line of sight are needed to reproduce the area asymmetry observed in the circular polarization profiles. In order to understand why both assumed geometries lead to similar properties for the penumbral fine structure, we have studied the sensitivity of the area asymmetry of selected spectral lines to discontinuities along the line of sight. The infrared lines used in this paper turn out to be almost insensitive to such gradients. This explains why the two-component model is able to provide a good fit to the observations and why inversions based on it reveal a very similar penumbral structure as the one-component model with gradients. The same sensitivity analysis carried out for visible lines commonly used in spectropolarimetry (Fe I 6301 and 6302 Å) indicates that the corresponding Stokes V profiles are much more asymmetric than their infrared counterparts. Therefore, it is very likely that models including gradients/discontinuities will be necessary to reproduce these lines.

We also point out that the results obtained from both assumed geometries can be naturally interpreted in terms of nearly horizontal flux tubes with a lower field strength containing outflowing gas that are embedded in a more vertical, stronger field in which gas is essentially at rest. This picture is in line with that proposed by Solanki & Montavon (1993) and Martínez Pillet (2000). The obvious next step is to carry out an inversion based on such a model. The most suitable spectropolarimetric data seems to be a combination of visible spectral lines sensitive to gradients along the line of sight and formed over a broad photospheric height range, and infrared lines that are highly sensitive to the magnetic field and formed deep in the solar photosphere.

The current work cannot contribute to the intense debate over the last years about the width of the flux tubes, in particular whether they are optically thick or thin (Sánchez Almeida 1998, 2001; Martínez Pillet 2000, 2001; Sütterlin 2001; Scharmer et al. 2002). The same observable effects would result from either one single thick tube (such as depicted in Fig. 9) or a bundle of smaller flux tubes of similar total optical thickness concentrated around $z \simeq 150$ km above the continuum layers. Recent observations of the penumbra at very high spatial resolution (Scharmer et al. 2002) show individual filaments 100−200 km thick (depending on whether only the inner dark core is considered to be a flux tube or the lateral bright features are also included). This strongly suggests that at our spatial resolution we deal with a situation where more than one fibril is present in the resolution element.

Acknowledgements. Manolo Collados and Manfred Schüssler are gratefully acknowledged for their continuous and stimulating discussions. L.B. is supported by the German Deutsche Forschungsgemeinschaft.

References

Barklem, P. S., & O'Mara, J. O. 1997, MNRAS, 290, 102
Barklem, P. S., O'Mara J. O., & Ross, J. E. 1998, MNRAS, 296, 1057
Bellot Rubio, L. R. 2003, in Third International Workshop on Solar Polarization, ed. J. Trujillo Bueno, & J. Sánchez Almeida, ASP Conf. Ser., 307, 301
Bellot Rubio, L. R., Ruiz Cobo, B., & Collados, M. 1998, ApJ, 506, 805
Bellot Rubio, L. R., Collados, M., Ruiz Cobo, B., et al. 2002, Il Nuovo Cimento C, 25, 543
Bellot Rubio, L. R., Balthasar, H., Collados, M., et al. 2003, A&A, 403, L47
Borrero, J. M., & Bellot Rubio, L. R. 2002, A&A, 385, 1056
Borrero, J. M., Bellot Rubio, L. R., Barklem, P. S., & del Toro Iniesta, J. C. 2003a, A&A, 404, 749
Borrero, J. M., Lagg, A., Solanki, S. K., et al. 2003b, in High Resolution Solar Observations: preparing for ATST, ed. A. Pevtstov, & H. Uitenbroek, ASP Conf. Ser., 286, 235
Degenhardt, D. 1989 A&A, 222, 297
Elmore, D. F., Lites, B. W., Tomczyk, S., et al. 1992, Proc. SPIE, 1746, 22
Frutiger, C., Solanki, S. K., Fligge, M., & Bruls, J. 1999, in Solar Polarization, ed. K. N. Nagendra, & J. O. Stenflo, Kluwer Academic Publishers (Astrophysics and space science library), 243, 281
Frutiger, C. 2000, Ph.D. Thesis, Institute of Astronomy, ETh Zürich, No. 13896
Grossmann-Doerth, U., Schüssler, M., & Solanki, S. K. 1989, A&A, 221, 338
Gustafsson, B. 1973, Upps. Astr. Obs. Ann. 5
Illing, R. M., Landman, D. A., & Mickey, D. L. 1974a, A&A, 35, 327
Illing, R. M., Landman, D. A., & Mickey, D. L. 1974b, A&A, 37, 97
Keppens, R., & Martínez Pillet, V. 1996, A&A, 316, 229
Landolfi, M., & degl'Innocenti, E. 1996, Sol. Phys., 164, 191
Leka, K. D., & Socas-Navarro, H. 2000, Bull. Am. Astron. Soc., 32, 804
Lites, B. W., & Skumanich, A. 1990, ApJ, 348, 747
Lites, B. W., Elmore, D. F., & Seagraves, P., et al. 1993, ApJ, 418, 928
Lites, B. W., Socas-Navarro, H., Skumanich, A., & Shimizu, T. 2002, ApJ, 575, 1131
Makita, M. 1986, Sol. Phys., 106, 269
Martínez Pillet, V. 2000, A&A, 361, 734
Martínez Pillet, V. 2001, A&A, 369, 644
Martínez Pillet, V., Collados, M., Bellot Rubio, L. R., et al. 1999, Mitt. Astron. Gesell., 15, 5
Mathew, S., Lagg, A., Solanki, S. K., et al. 2003, A&A, 410, 695
Mathew, S., Solanki, S. K., Lagg, A., et al. 2004, A&A, 422, 693
McPherson, M. R., Lin, H., & Kuhn, K. R. 1992, Sol. Phys., 139, 255
Meyer, F., & Schmidt, H. U. 1968, Z. Ang. Math. Mech., 48, T218
Montesinos, B., & Thomas, J. 1993, ApJ, 402, 314
Montesinos, B., & Thomas, J. 1997, Nature, 390, 485
Müller, D. A. N., Schlichenmaier, R., Steiner, O., & Stix, M. 2002, A&A, 393, 305
Press, W. H., Flannery, B. P., Teukolsky, S. A., & Vetterling, W. T. 1986, Numerical Recipes (Cambridge Univ. Press)
Rüedi, I., Solanki, S. K., Keller, C. U., & Frutiger, C. 1998, A&A, 338, 1089
Rüedi, I., Solanki, S. K., & Keller, C. U. 1999, A&A, 348, L37
Ruiz Cobo, B. 1998, Ap&SS, 263, 331
Ruiz Cobo, B., & del Toro Iniesta, J. C. 1992, ApJ, 398, 375
Sánchez Almeida, J. 1998, ApJ, 497, 967
Sánchez Almeida, J. 2001, A&A, 369, 643
Sánchez Almeida, J., & Lites, B. 1992, ApJ, 398, 359
Scharmer, G., Gudiksen, B. V., Kiselman, D., et al. 2002, Nature, 420, 151

Schlichenmaier, R. 2002, AN, 323, 303
Schlichenmaier, R., & Collados, M. 2002, A&A, 381, 668
Schlichenmaier, R., Jahn, K., & Schmidt, H. U. 1998a, ApJ, 493, L121
Schlichenmaier, R., Jahn, K., & Schmidt, H. U. 1998b, A&A, 337, 897
Schlichenmaier, R., Müller, D. A. N., Steiner, O., & Stix, M. 2002, A&A, 381, L77
Skumanich, A., & Lites, B. W. 1987, ApJ, 322, 473
Socas-Navarro, H. 2001, in Advanced Solar Polarimetry; Theory, Observations and Instrumentation, ed. Michael Sigwarth, ASP Conf. Ser., 236, 487
Solanki, S. K. 2003, A&AR, 11, 153
Solanki, S. K., & Montavon, C. A. P. 1993, A&A, 275, 283
Solanki, S. K., & Schmidt, H. U. 1993, A&A, 267, 287
Solanki, S. K., Rüedi, I., & Livingston, W. 1992, A&A, 263, 339
Solanki, S. K., Walther, U., & Livingston, W. 1993, A&A, 277, 639
Solanki, S. K., Montavon, C. A. P., & Livingston, W. 1994, A&A, 283, 221
Solanki, S. K., Finsterle, W., Rüedi, I., & Livingston, W. 1999, A&A, 347, L27
Stanchfield, D. C. H., Thomas, J. H., & Lites, B. W. 1997, ApJ, 477, 485
Sütterlin, P. 2001, A&A, 374, L21
Thomas, J. 1988, ApJ, 333, 407
Thomas, J., & Montesinos, B. 1990, ApJ, 359, 550
Thomas, J., & Montesinos, B. 1991, ApJ, 375, 404
Title, A. M., Frank, Z. A., Shine, R. A., et al. 1993, ApJ, 403, 780
del Toro Iniesta, J. C. 2003, Astron. Nachr., 324, 383
del Toro Iniesta, J. C., Tarbell, T. D., & Ruiz Cobo, B. 1994, ApJ, 436, 400
del Toro Iniesta, J. C., Bellot Rubio, L. R., & Collados, M. 2001, ApJ, 549, L139
Westendorp Plaza, C., del Toro Iniesta, J. C., Ruiz Cobo, B., et al. 1997, Nature, 389, 47
Westendorp Plaza, C., del Toro Iniesta, J. C., Ruiz Cobo, B., et al. 1998, ApJ, 494, 453
Westendorp Plaza, C., del Toro Iniesta, J. C., Ruiz Cobo, B., & Martínez Pillet, V. 2001a, ApJ, 547, 1148
Westendorp Plaza, C., del Toro Iniesta, J. C., Ruiz Cobo, B., et al. 2001b, ApJ, 547, 1130